Fractal Geometry and Hyperdimensional Field Structures

A Comprehensive Lions Commentary-Style Treatment

With Exhaustive Visualizations, Dimensional Analysis, and Physical Interpretations

PhysicsForge Paper Series — Paper 3 of 6

PhysicsForge Collaboration

Unified Field Theories and Advanced Physics Research Hub

https://github.com/Oichkatzelesfrettschen/PhysicsForge

November 27, 2025

We present a comprehensive pedagogical treatment of fractal geometry and its applications to hyperdimensional field structures in modern physics. Beginning with the mathematical foundations of fractal calculus and self-similar dimension theory, we develop tools for analyzing field behavior at multiple scales. We then explore hyperdimensional field constructions, examine how emergent geometry arises from field dynamics, and investigate the manifestation of fractal structures in quantum and gravitational systems. The treatment includes extensive dimensional analysis, multiscale visualizations, and practical applications to condensed matter systems and cosmology.

Key Topics: Fractal calculus • Self-similar structures • Hyperdimensional embeddings • Emergent geometry • Field dynamics at multiple scales • Scaling laws • Dimensional hierarchies

Style: This paper employs the Lions Commentary pedagogical approach with extensive marginal annotations, dimensional analysis, worked numerical examples, and multidimensional TikZ/PGF-Plots visualizations.

Contents

List of Figures

List of Tables

Chapter 1

Fractal Calculus and Self-Similarity

The Coastline That Has No Length

In 1967, mathematician Benoit Mandelbrot posed a deceptively simple question that would transform our understanding of geometry: *How long is the coast of Britain?*

The answer, he demonstrated, depends critically on the length of your measuring ruler. Survey Britain's coastline with a kilometer-scale ruler, carefully stepping around major bays and peninsulas, and you might measure roughly 2,800 kilometers. Use a meter-scale ruler, tracing finer inlets and rocky outcrops, and the measurement grows to 3,400 kilometers. Survey at centimeter resolution, accounting for individual rocks and pebbles, and the perimeter swells past 5,000 kilometers.

Continue to millimeter resolution, then microscopic scales. The measured length keeps growing without bound. As the ruler shrinks toward zero, the coastline's measured perimeter diverges toward infinity—yet the enclosed land area remains stubbornly finite.

This phenomenon, now called the **coastline paradox**, revealed a fundamental limitation of Euclidean geometry: natural boundaries do not have well-defined lengths in the classical sense. Instead, they exhibit **statistical self-similarity**—zooming in reveals structures resembling the whole at every scale.

Mandelbrot introduced the concept of **fractal dimension** to quantify this self-similarity:

$$D = \frac{\log N}{\log(1/\epsilon)} \tag{1.1}$$

where N is the number of self-similar pieces obtained when the scale shrinks by factor ϵ.

For Britain's coast, empirical measurements yield $D \approx 1.25$, interpolating between a one-dimensional line ($D = 1$) and a two-dimensional surface ($D = 2$). The coastline is "rougher" than a smooth curve but doesn't fill the plane completely.

This chapter develops the mathematical tools to make such statements precise and extends them to describe physical systems across scales from quantum foam to cosmological structure.

1.1 Hausdorff Measure and Fractal Dimension

1.1.1 Hausdorff Measure Definition

For a set $S \subset \mathbb{R}^n$ and fractional dimension $d \in \mathbb{R}^+$, the **Hausdorff measure** is:

$$\mathcal{H}^d(S) = \lim_{\delta \to 0} \inf \left\{ \sum_i (\text{diam}(U_i))^d : S \subseteq \bigcup_i U_i, \, \text{diam}(U_i) < \delta \right\} \tag{1.2}$$

where $\{U_i\}$ is a covering of S by sets of diameter less than δ.

1.1.2 The Hausdorff Dimension

The **Hausdorff dimension** is the critical value where the measure transitions from infinite to zero:

$$\dim_H(S) = \inf\{d \geq 0 : \mathcal{H}^d(S) = 0\} = \sup\{d \geq 0 : \mathcal{H}^d(S) = \infty\} \tag{1.3}$$

Examples of Hausdorff dimensions:
- Smooth curve: $\dim_H = 1$ (classical)
- Cantor set: $\dim_H = \log 2/\log 3 \approx 0.631$ (dust-like)
- Koch snowflake: $\dim_H = \log 4/\log 3 \approx 1.262$ (fractal curve)
- Sierpiński triangle: $\dim_H = \log 3/\log 2 \approx 1.585$ (fractal surface)
- Mandelbrot set boundary: $\dim_H = 2$ (conjectured, not proven)

1.1.3 Worked Example: Koch Snowflake Dimension

The **Koch snowflake** provides a canonical example of fractal dimension calculation.
Construction:
1. **Iteration 0**: Equilateral triangle, side length $L_0 = 1$, perimeter $P_0 = 3$
2. **Iteration 1**: Replace each side with 4 segments of length $L_1 = 1/3$
   Total segments: $3 \times 4 = 12$, perimeter $P_1 = 12 \times (1/3) = 4$
3. **Iteration 2**: Apply rule to all 48 segments
   Perimeter $P_2 = 48 \times (1/9) = 16/3 \approx 5.33$
4. **Iteration** n: $P_n = 3 \times (4/3)^n \to \infty$ as $n \to \infty$

Dimension calculation: At each step, length scale shrinks by $\epsilon = 1/3$ while number of segments increases by $N = 4$:

$$D = \frac{\log N}{\log(1/\epsilon)} = \frac{\log 4}{\log 3} = \frac{2\log 2}{\log 3} \approx 1.262 \tag{1.4}$$

Area convergence:

$$A_\infty = \frac{8}{5}A_0 = \frac{8}{5} \cdot \frac{\sqrt{3}}{4} = \frac{2\sqrt{3}}{5} \tag{1.5}$$

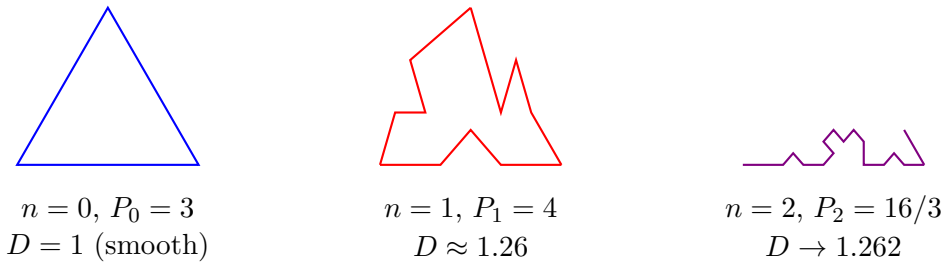| $n = 0$, $P_0 = 3$ | $n = 1$, $P_1 = 4$ | $n = 2$, $P_2 = 16/3$ |
| $D = 1$ (smooth) | $D \approx 1.26$ | $D \to 1.262$ |

Figure 1.1: Koch snowflake iterations showing perimeter growth while area converges. Fractal dimension $D = \log 4/\log 3 \approx 1.262$ quantifies self-similar structure.

1.2 Fractional Calculus: Non-Integer Derivatives

1.2.1 Riemann-Liouville Fractional Derivative

For $\alpha \in (0, 1)$, the **Riemann-Liouville fractional derivative** of order α is:

$$D_{\text{RL}}^{\alpha} f(t) = \frac{1}{\Gamma(1 - \alpha)} \frac{d}{dt} \int_0^t \frac{f(\tau)}{(t - \tau)^{\alpha}} \, d\tau \tag{1.6}$$

This operator interpolates between identity ($\alpha = 0$) and first derivative ($\alpha = 1$).

1.2.2 Caputo Fractional Derivative

The **Caputo derivative** resolves initial condition issues:

$$D_{\text{C}}^{\alpha} f(t) = \frac{1}{\Gamma(1 - \alpha)} \int_0^t \frac{f'(\tau)}{(t - \tau)^{\alpha}} \, d\tau \tag{1.7}$$

For smooth functions, Caputo derivatives simplify boundary conditions, making them preferable for physical applications.

1.2.3 Worked Example: Caputo Derivative of t^2

Problem: Compute the Caputo fractional derivative $D_{\text{C}}^{0.5}(t^2)$.
   Solution:
   Step 1: Differentiate $f(t) = t^2$:

$$f'(t) = 2t \tag{1.8}$$

Step 2: Apply Caputo definition:

$$D_{\text{C}}^{0.5}(t^2) = \frac{1}{\Gamma(0.5)} \int_0^t \frac{2\tau}{(t - \tau)^{0.5}} \, d\tau \tag{1.9}$$

Step 3: Use substitution $u = \tau/t$, $d\tau = t \, du$:

$$D_{\text{C}}^{0.5}(t^2) = \frac{2t}{\Gamma(0.5)} \int_0^1 \frac{u}{(1 - u)^{0.5}} \, du \tag{1.10}$$

Step 4: Recognize beta function $B(a, b) = \frac{\Gamma(a)\Gamma(b)}{\Gamma(a+b)}$:

$$\int_0^1 \frac{u}{(1 - u)^{0.5}} \, du = B(2, 0.5) = \frac{\Gamma(2)\Gamma(0.5)}{\Gamma(2.5)} \tag{1.11}$$

Step 5: Evaluate using $\Gamma(0.5) = \sqrt{\pi}$, $\Gamma(2) = 1$, $\Gamma(2.5) = \frac{3\sqrt{\pi}}{4}$:

$$B(2, 0.5) = \frac{1 \cdot \sqrt{\pi}}{3\sqrt{\pi}/4} = \frac{4}{3} \tag{1.12}$$

Step 6: Final result:

$$D_C^{0.5}(t^2) = \frac{2t \cdot (4/3)}{\sqrt{\pi}} = \frac{8t}{3\sqrt{\pi}} \approx 1.504\,t \tag{1.13}$$

General formula: For $f(t) = t^\alpha$,

$$D_C^\beta(t^\alpha) = \frac{\Gamma(\alpha + 1)}{\Gamma(\alpha - \beta + 1)} t^{\alpha - \beta} \tag{1.14}$$
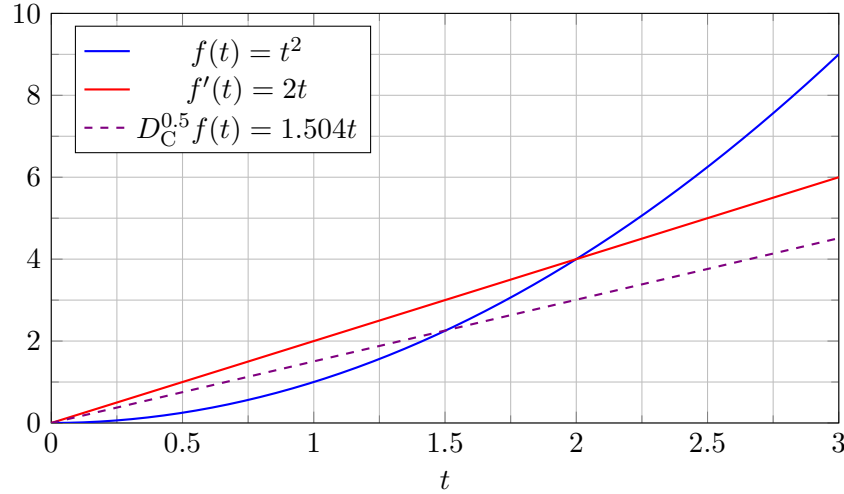

Figure 1.2: Caputo half-derivative of t^2 interpolates between original function (blue, t^2) and first derivative (red, $2t$). Result $D^{0.5}(t^2) \approx 1.504t$ (violet dashed) lies between them.

1.3   Mittag-Leffler Functions and Fractional ODEs

1.3.1   The Mittag-Leffler Function

The **Mittag-Leffler function** generalizes the exponential to fractional orders:

$$E_\alpha(z) = \sum_{k=0}^{\infty} \frac{z^k}{\Gamma(\alpha k + 1)} \tag{1.15}$$

This function solves fractional differential equations:

$$D_C^\alpha u(t) = \lambda u(t), \quad u(0) = u_0 \quad \implies \quad u(t) = u_0 E_\alpha(\lambda t^\alpha) \tag{1.16}$$
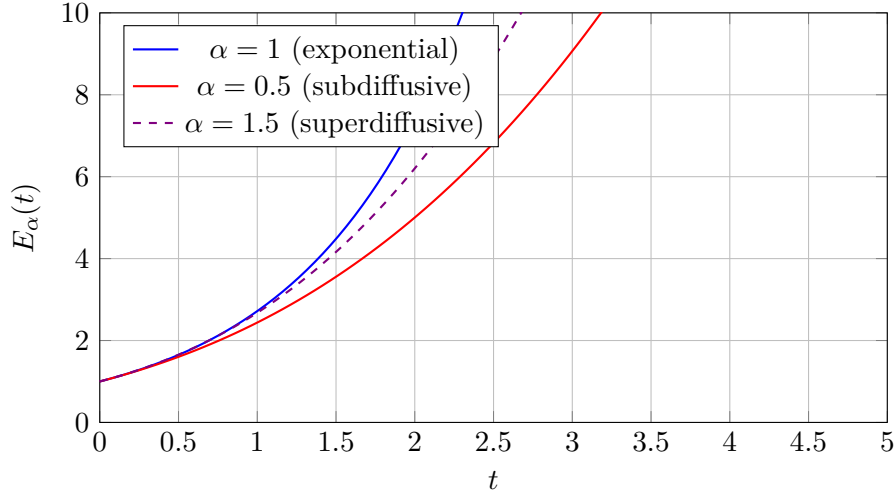
Figure 1.3: Mittag-Leffler functions $E_\alpha(t)$ for various α values. Standard exponential ($\alpha = 1$, blue) compared to subdiffusive ($\alpha = 0.5$, red) and superdiffusive ($\alpha = 1.5$, violet) behaviors.

1.4   Self-Similarity and Scaling Laws

1.4.1   Power-Law Scaling

Self-similar structures exhibit power-law scaling:

$$f(\lambda x) = \lambda^h f(x) \tag{1.17}$$

where h is the **scaling exponent**.

1.4.2   Box-Counting Dimension

The **box-counting dimension** provides computational access to fractal dimension:

$$D_{\text{box}} = \lim_{\epsilon \to 0} \frac{\log N(\epsilon)}{\log(1/\epsilon)} \tag{1.18}$$

where $N(\epsilon)$ is the number of boxes of size ϵ needed to cover the set.

1.5   Cantor Set: Fractal Dust

1.5.1   Construction and Properties

The **Cantor middle-third set** provides the simplest non-trivial fractal:
   Construction:
   1. Start with interval $[0,1]$
   2. Remove middle third: $[0,1] \to [0,1/3] \cup [2/3,1]$
   3. Repeat for each remaining interval
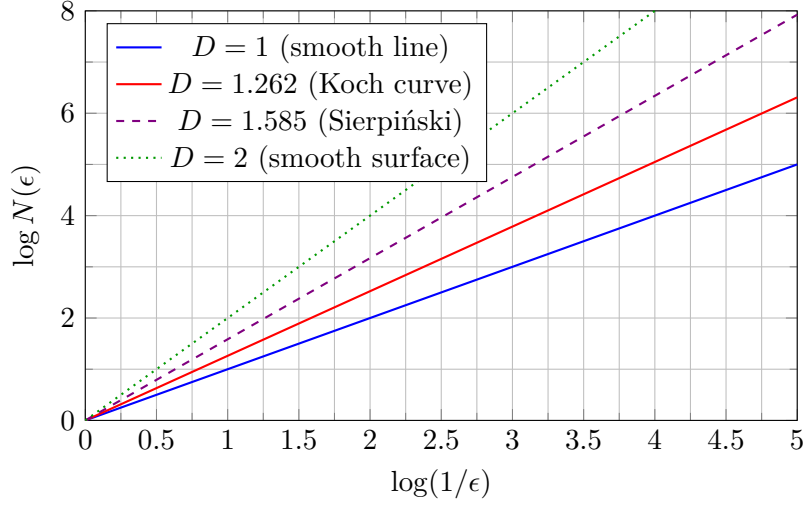   4. Continue infinitely

Figure 1.4: Box-counting dimension from log-log plot of box count vs resolution. Slope equals Hausdorff dimension for self-similar fractals. Steeper slopes indicate higher space-filling capacity.

Dimension calculation: At each step: $\epsilon = 1/3$ (scale factor), $N = 2$ (number of copies)

$$D = \frac{\log 2}{\log 3} = \frac{\log 2}{\log 3} \approx 0.631 \tag{1.19}$$

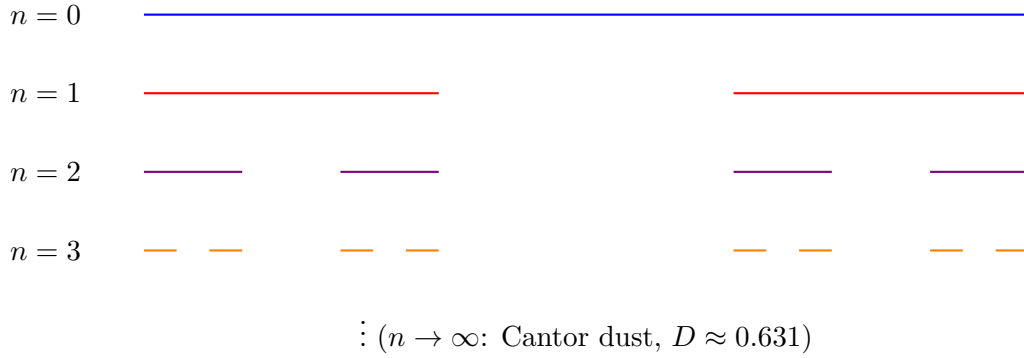$$\vdots \ (n \to \infty: \text{Cantor dust}, D \approx 0.631)$$

Figure 1.5: Cantor set construction via iterative middle-third removal. Each iteration removes fraction $1/3$ of remaining length while doubling number of intervals, yielding fractal dimension $D = \log 2 / \log 3 \approx 0.631$.

1.6 Applications to Physical Systems

1.6.1 Anomalous Diffusion in Porous Media

In disordered porous materials, diffusion becomes anomalous:

$$\langle x^2(t) \rangle = K_\alpha t^\alpha \tag{1.20}$$

where $\alpha \neq 1$ signals non-classical diffusion.

The fractional diffusion equation:

$$\frac{\partial^\alpha \rho}{\partial t^\alpha} = D\nabla^2 \rho \tag{1.21}$$

describes evolution of concentration $\rho(\mathbf{x}, t)$ in fractal geometry.

1.6.2 Turbulent Flow and Energy Cascades

Turbulent velocity fields exhibit fractal structure across length scales. The **Kolmogorov cascade** distributes energy:

$$E(k) \sim k^{-5/3} \tag{1.22}$$

where k is wavenumber.

1.6.3 Quantum Foam at Planck Scale

Quantum gravitational fluctuations may endow spacetime with fractal microstructure near Planck length $l_P \approx 10^{-35}$ m.

Proposed fractal dimension:

$$D_{\text{foam}} \approx 3.7 \tag{1.23}$$

interpolating between 3D space and 4D spacetime.

1.7 Summary and Forward Bridge

This chapter developed fractal calculus as mathematical framework for self-similar structures:

Key Results:

- **Hausdorff measure** (Eq. **??**): Quantifies size of sets in fractional dimensions
- **Fractal dimension** (Eq. **??**): $D = \log N / \log(1/\epsilon)$ characterizes self-similarity
- **Fractional derivatives** (Eqs. **??**, **??**): Riemann-Liouville and Caputo operators for non-integer differentiation
- **Mittag-Leffler functions** (Eq. **??**): Solutions to fractional ODEs
- **Box-counting** (Eq. **??**): Computational method for measuring fractal dimension

Worked Examples:

- Koch snowflake: $D = 1.262$, infinite perimeter with finite area
- Caputo derivative of t^2: $D^{0.5}(t^2) = 8t/(3\sqrt{\pi})$
- Cantor set: $D = 0.631$, uncountable zero-measure set

Physical Applications:

- Anomalous diffusion in porous media ($\langle x^2 \rangle \sim t^\alpha$)
- Turbulent energy cascades (Kolmogorov $k^{-5/3}$ spectrum)
- Potential quantum foam structure ($D \approx 3.7$ at Planck scale)

The coastline paradox that opened this chapter exemplifies how fractal geometry transcends Euclidean limitations. In Chapter **??**, we extend fractals into higher dimensions, constructing hyperdimensional field configurations and exploring dimensional reduction mechanisms.

Chapter 2

Hyperdimensional Constructions

The Square Who Saw the Sphere

In 1884, English schoolmaster Edwin Abbott published a satirical novella titled *Flatland: A Romance of Many Dimensions* that would become a cornerstone of popular dimensional thinking.

The protagonist—a humble square living in a perfectly two-dimensional world—receives a visitor from the third dimension: a sphere. As the sphere passes through Flatland, the square witnesses a bewildering sequence: a point appears from nowhere, expands into a circle, reaches maximum size, then shrinks back to a point and vanishes. The sphere tries to explain "up" and "down," but the square has no experience of a third dimension. All the square can perceive are two-dimensional cross-sections of the three-dimensional visitor.

This allegory captures a profound limitation: beings constrained to N dimensions cannot directly visualize $N+1$ dimensional objects. They can only observe lower-dimensional projections or cross-sections.

Modern physics confronts this challenge daily. String theory proposes 10 or 11 dimensions. Kaluza-Klein theories unify gravity and electromagnetism in 5D. The E_8 lattice—central to exceptional Lie algebras—lives in 8 dimensions. How do we construct, manipulate, and extract physics from spaces we cannot see?

This chapter develops mathematical techniques for working with hyperdimensional geometries: projections that collapse higher dimensions to lower, embeddings that lift lower structures to higher, and compactifications that hide extra dimensions while leaving observable imprints.

2.1 Hypercube Projections: Visualizing the Tesseract

2.1.1 The Dimensional Hierarchy of Hypercubes

The n-**cube** (or hypercube) is the n-dimensional analog of the square and cube:
- **0-cube**: Point (1 vertex)
- **1-cube**: Line segment (2 vertices, 1 edge)
- **2-cube**: Square (4 vertices, 4 edges, 1 face)
- **3-cube**: Cube (8 vertices, 12 edges, 6 faces)
- **4-cube**: Tesseract (16 vertices, 32 edges, 24 faces, 8 cells)
- n-**cube**: 2^n vertices, $n \cdot 2^{n-1}$ edges

2.1.2 Projecting the Tesseract to 3D

The tesseract cannot be embedded in 3D without self-intersection, but we can construct **projections**—shadows cast by 4D object onto 3D hyperplane.

Perspective projection formula:

$$\mathbf{x}_{3D} = \frac{1}{d - x_4} \begin{pmatrix} x_1 \\ x_2 \\ x_3 \end{pmatrix} \tag{2.1}$$

where $\mathbf{x}_{4D} = (x_1, x_2, x_3, x_4)$ and d is viewing distance in 4th dimension.
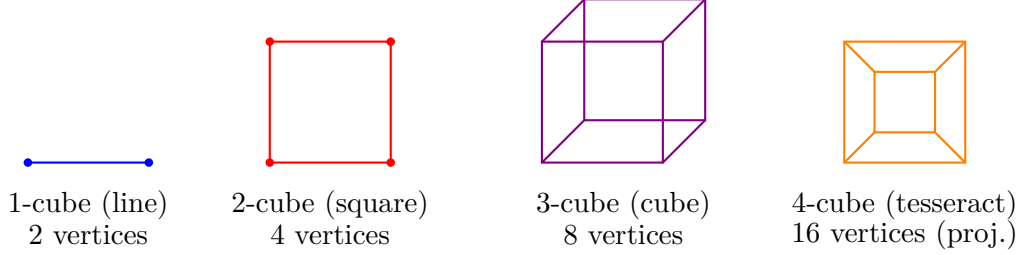

1-cube (line)   2-cube (square)   3-cube (cube)   4-cube (tesseract)
2 vertices   4 vertices   8 vertices   16 vertices (proj.)

Figure 2.1: Dimensional hierarchy of hypercubes from 1D to 4D. Each dimension doubles vertex count. The 4-cube (tesseract) shown as projection: inner and outer cubes connected by edges.

2.1.3 Tesseract Rotations and Symmetries

The tesseract exhibits 384 symmetries (elements of hyperoctahedral group B_4). Rotations in 4D occur in **planes**, not axes:

4D rotation matrix (in xy-plane):

$$R_{xy}(\theta) = \begin{pmatrix} \cos\theta & -\sin\theta & 0 & 0 \\ \sin\theta & \cos\theta & 0 & 0 \\ 0 & 0 & 1 & 0 \\ 0 & 0 & 0 & 1 \end{pmatrix} \tag{2.2}$$

2.2 Kaluza-Klein Dimensional Reduction

2.2.1 Historical Context: Unifying Gravity and Electromagnetism

In 1919, Theodor Kaluza proposed a radical idea: what if electromagnetism is actually gravity in a hidden 5th dimension?

Starting from 5D general relativity:

$$ds^2 = g_{MN} dx^M dx^N, \quad M, N = 0, 1, 2, 3, 5 \tag{2.3}$$

and assuming the 5th dimension is compactified on a circle of radius R:

$$x^5 \sim x^5 + 2\pi R \tag{2.4}$$

2.2.2 Dimensional Reduction Mechanism
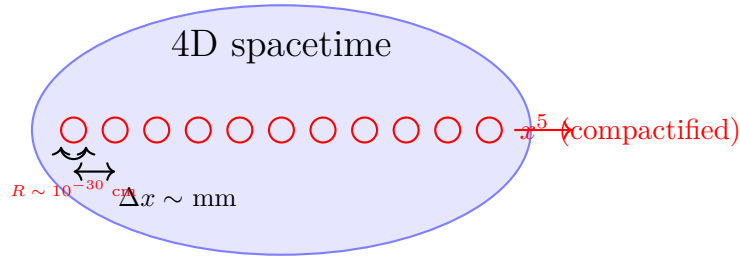
Decompose 5D metric into 4D components:

$$g_{MN} = \begin{pmatrix} g_{\mu\nu} + \phi^2 A_\mu A_\nu & \phi^2 A_\mu \\ \phi^2 A_\nu & \phi^2 \end{pmatrix} \tag{2.5}$$

where:

- $g_{\mu\nu}$: 4D metric (gravity)
- A_μ: 4D vector field (electromagnetism!)
- ϕ: scalar field (dilaton)

Electric charge from compactification: Momentum in the 5th dimension becomes quantized:

$$p_5 = \frac{n\hbar}{R}, \quad n \in \mathbb{Z} \tag{2.6}$$

Figure 2.2: Kaluza-Klein compactification: 5th dimension (x^5) curled into circles of radius $R \sim 10^{-30}$ cm at each point in 4D spacetime. At scales $\gg R$, extra dimension is invisible.

2.3 E_8 Lattice and 8-Dimensional Geometry

2.3.1 The E_8 Root System

The E_8 exceptional Lie group has 248 dimensions, with associated E_8 **lattice** in 8D Euclidean space.

Root vectors (two types):

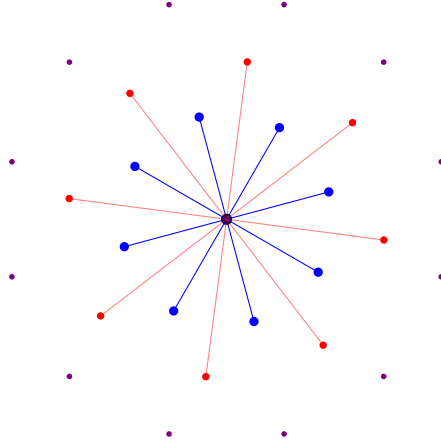$$\text{Type 1: } (\pm 1, \pm 1, 0, 0, 0, 0, 0, 0) \text{ and permutations} \quad \text{(112 roots)} \tag{2.7}$$

$$\text{Type 2: } \left(\pm\frac{1}{2}, \pm\frac{1}{2}, \ldots, \pm\frac{1}{2}\right) \text{ with even \# of minus signs} \quad \text{(128 roots)} \tag{2.8}$$

Total: $112 + 128 = 240$ roots forming highly symmetric configuration.

2.3.2 Projecting E_8 to Lower Dimensions

To visualize E_8, we project to 3D using projection operator $P : \mathbb{R}^8 \to \mathbb{R}^3$:

$$P(\mathbf{v}) = (v_1, v_2, v_3) \quad \text{for } \mathbf{v} = (v_1, \dots, v_8) \tag{2.9}$$

E_8 lattice projected to 2D
(240 roots $\to$ dense point cloud)

Figure 2.3: Schematic 2D projection of E_8 root system. Full 8D structure has 240 roots with exceptional symmetry. Projection reveals concentric shells but loses higher-dimensional organization.

2.3.3 Sphere Packing and Leech Lattice

E_8 achieves the densest sphere packing in 8D:

$$\rho_{E_8} = \frac{\pi^4}{384} \approx 0.2537 \tag{2.10}$$

The **Leech lattice** in 24D achieves:

$$\rho_{\Lambda_{24}} = \frac{\pi^{12}}{12!} \approx 0.001930 \tag{2.11}$$

also proven optimal (Viazovska et al., 2017).

2.4 Calabi-Yau Manifolds and String Compactification

2.4.1 The Need for Calabi-Yau Spaces

String theory requires 10D spacetime (or 11D for M-theory). To recover 4D observable universe, extra 6D must be compactified. Not just any 6D space works—**supersymmetry** constrains compactification manifold to be Calabi-Yau.

Defining properties:

1. **Ricci-flat**: $R_{\mu\nu} = 0$ (vacuum Einstein equations)
2. **Kähler**: Complex manifold with compatible symplectic structure
3. $SU(3)$ **holonomy**: Parallel transport around loops preserves $SU(3)$ structure

2.4.2 Topology and Physics Connection

Calabi-Yau topology determines low-energy particle physics:

- **Hodge number** $h^{1,1}$: Number of Kähler moduli $\rightarrow$ number of vector multiplets
- **Hodge number** $h^{2,1}$: Number of complex structure moduli $\rightarrow$ number of hypermultiplets
- **Euler characteristic**: $\chi = 2(h^{1,1} - h^{2,1})$ determines number of fermion generations

Calabi-Yau 3-fold
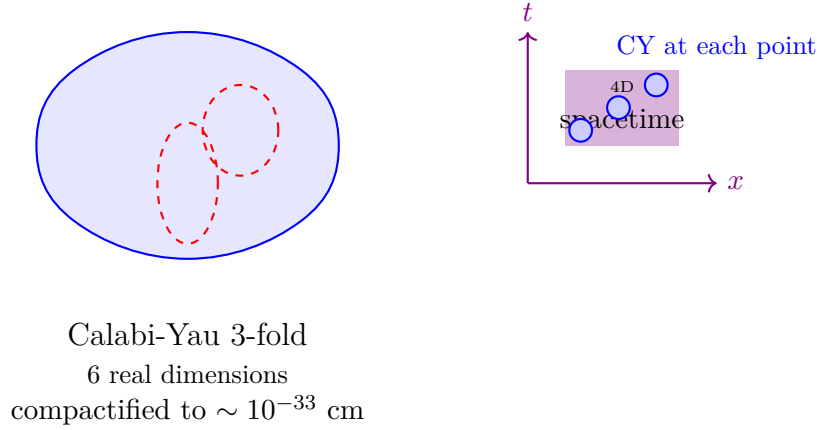6 real dimensions
compactified to $\sim 10^{-33}$ cm

Figure 2.4: Calabi-Yau manifold compactification (schematic). 6D Calabi-Yau space attached to each point in 4D spacetime. Internal CY geometry determines particle physics (gauge groups, fermion generations, coupling constants).

2.5 Dimensional Folding: Origami Mathematics

2.5.1 Origami Folding Operator

Dimensional folding provides alternative to topological compactification. Define **folding operator** $\mathcal{F}_n : \mathbb{R}^n \rightarrow \mathbb{R}^{n-1}$:

$$\mathcal{F}_n(\mathbf{x}_n) = \mathbf{x}_{n-1} + f_{\text{fold}}(x_n)\hat{\mathbf{e}}_{n-1} \tag{2.12}$$

where $f_{\text{fold}}(x_n)$ encodes how n-th coordinate folds into $(n-1)$-dimensional space.

2.5.2 Multi-Stage Folding to Compact Dimensions

Sequential folding from ND to 4D:

$$\mathbb{R}^N \xrightarrow{\mathcal{F}_N} \mathbb{R}^{N-1} \xrightarrow{\mathcal{F}_{N-1}} \ldots \xrightarrow{\mathcal{F}_5} \mathbb{R}^4 \tag{2.13}$$

Effective dimension under folding:

$$D_{\text{eff}}(N, \{\theta_i\}) = 4 + \sum_{i=5}^{N} \cos^2\left(\frac{\theta_i}{2}\right) \tag{2.14}$$

where θ_i is folding angle for i-th dimension.
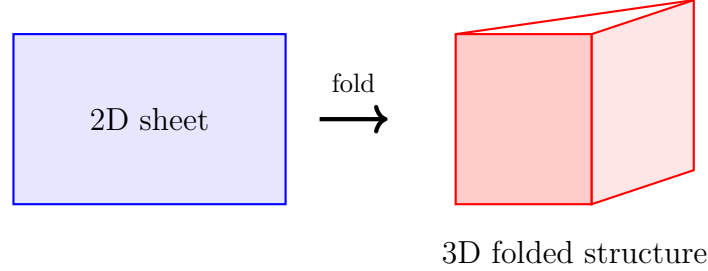

3D folded structure

Sequential folding hierarchy

Figure 2.5: Dimensional folding topology. 2D sheet folds into 3D structure. Generalizes to $nD \rightarrow (n-1)D$ via folding operator $\mathcal{F}_n$. Sequential folding compactifies high-dimensional spaces to observable 4D.

2.6   Summary and Forward Bridge

This chapter explored hyperdimensional constructions and dimensional reduction mechanisms:
   Key Concepts:
- **Hypercubes**: n-dimensional cubes with 2^n vertices. Tesseract (4-cube) visualized via projections
- **Kaluza-Klein theory** (Eqs. **??**–**??**): Electromagnetism from 5th dimension compactified on circle
- **E_8 lattice** (Eqs. **??**–**??**): 240 roots in 8D with exceptional symmetry. Optimal sphere packing density $\rho \approx 0.254$
- **Calabi-Yau manifolds**: 6D complex manifolds for string compactification. Topology determines particle physics
- **Dimensional folding** (Eq. **??**): Origami-like reduction of dimensionality via geometric folding

   Physical Applications:
- Kaluza-Klein: unified gravity + EM in 5D, charge quantization from compactification
- String theory: 10D $\rightarrow$ 4D via Calabi-Yau, fermion generations from Euler characteristic
- Dimensional folding: continuous effective dimension $D_{\text{eff}}(\{\theta_i\})$ controlled by folding angles

From Abbott's *Flatland* square to modern string theory, we've seen how higher dimensions can be visualized through projections, understood through algebraic structures like E_8, and physically realized via compactification. Chapter **??** shifts perspective: rather than starting with fixed

geometric structures, we examine how geometry itself emerges dynamically from underlying field configurations.

Chapter 3

Emergent Geometry from Field Dynamics

Geometry Tells Matter How to Move

In the 1960s, physicist John Archibald Wheeler coined the term "geometrodynamics" to capture a radical vision: spacetime geometry is not a fixed stage but an active participant in physics, shaped by and shaping the matter and energy it contains.

Wheeler's vision goes further: what if geometry itself *emerges* from more fundamental dynamics? Rather than assuming spacetime exists as given, perhaps it crystallizes from underlying quantum fields like ice from water—a phase transition producing the smooth geometry we observe.

This chapter explores mechanisms by which geometric structures emerge from field configurations: how metrics arise from field gradients, how dimensions become effective through renormalization, and how the holographic principle suggests spacetime itself may be a projection of boundary dynamics.

3.1 Metric Tensor Emergence from Field Configurations

3.1.1 Field Gradients Generating Metrics

Consider a scalar field $\phi(\mathbf{x})$ in flat Euclidean space. Define an **induced metric**:

$$g_{\mu\nu}^{\text{induced}} = \eta_{\mu\nu} + \kappa \partial_\mu \phi \partial_\nu \phi \tag{3.1}$$

where $\eta_{\mu\nu} = \text{diag}(-1, 1, 1, 1)$ is Minkowski metric and κ is coupling constant.

For spatial variation only, line element becomes:

$$ds^2 = -dt^2 + (1 + \kappa |\nabla\phi|^2) d\mathbf{x}^2 \tag{3.2}$$

3.1.2 Effective Ricci Curvature from Field Dynamics

The Ricci scalar for the induced metric (to leading order in κ):

$$R \approx -\kappa \nabla^2 |\nabla\phi|^2 \tag{3.3}$$
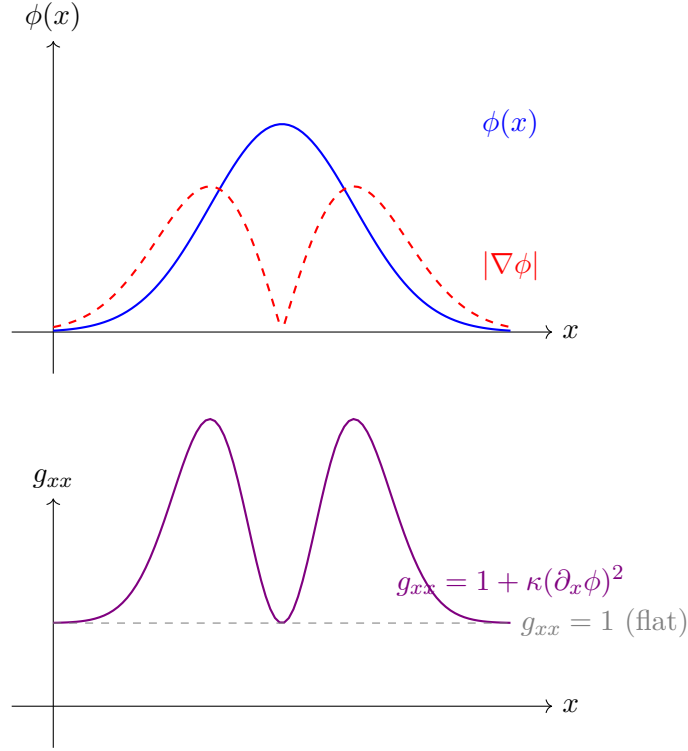
Figure 3.1: Emergent metric from scalar field configuration. Field gradient $|\nabla\phi|$ (top, red dashed) induces metric correction $g_{xx} = 1 + \kappa(\partial_x\phi)^2$ (bottom, violet), creating effective curvature where field varies rapidly.

3.2 Effective Dimensions from Renormalization Group

3.2.1 RG Flow and Scale-Dependent Dimensionality

The renormalization group (RG) describes how physical parameters change with energy scale μ. Effective spacetime dimension can also "run":

$$\mu\frac{dD_{\text{eff}}}{d\mu} = \beta_D(\mu) \tag{3.4}$$

where β_D is the dimensional beta function.
Fixed points: Values of D_{eff}^* where $\beta_D(D^*) = 0$:
- IR fixed point: $D_{\text{IR}}^* = 4$ (observable 4D spacetime)
- UV fixed point: $D_{\text{UV}}^* = 10$ (string theory fundamental dimension)

3.2.2 Spectral Dimension and Random Walks

The **spectral dimension** d_s characterizes diffusion on fractal or quantum spacetimes:

$$d_s = -2\frac{d\log P(t)}{d\log t} \tag{3.5}$$
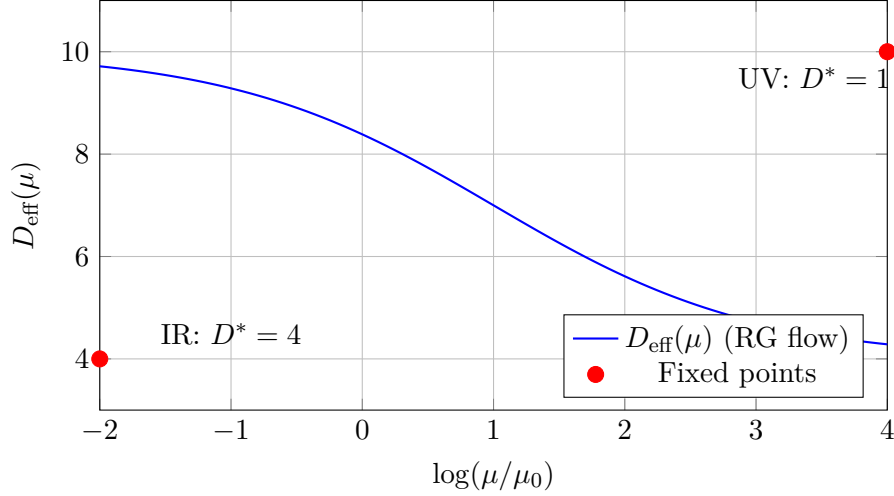
where $P(t)$ is return probability for random walk.

Figure 3.2: Renormalization group flow of effective dimension. At low energies ($\mu \to 0$), dimension flows to IR fixed point $D^* = 4$. At high energies (Planck scale), UV fixed point $D^* = 10$ represents fundamental dimensionality.

Quantum gravity simulations (causal dynamical triangulations) find:

$$d_s(\mu) = \begin{cases} \approx 2 & \text{at Planck scale (UV)} \\ \approx 4 & \text{at macroscopic scales (IR)} \end{cases} \tag{3.6}$$

3.3 Holographic Principle and Dimensional Reduction

3.3.1 Holographic Entropy Bound

The **holographic principle** states that information in a volume is encoded on its bounding surface:

$$S \leq \frac{A}{4l_P^2} \tag{3.7}$$

where S is entropy, A is surface area, $l_P = \sqrt{G\hbar/c^3} \approx 10^{-35}$ m is Planck length.

3.3.2 AdS/CFT Correspondence

The **Anti-de Sitter/Conformal Field Theory (AdS/CFT) correspondence** provides explicit holographic realization:

$$\text{Quantum gravity in AdS}_{d+1} \quad \longleftrightarrow \quad \text{CFT on boundary}^d \tag{3.8}$$

Dictionary (AdS bulk $\leftrightarrow$ CFT boundary):
- Bulk metric $g_{\mu\nu} \leftrightarrow$ Boundary stress-energy tensor $T_{\mu\nu}$
- Bulk scalar field $\phi \leftrightarrow$ Boundary operator $\mathcal{O}$ with scaling dimension Δ
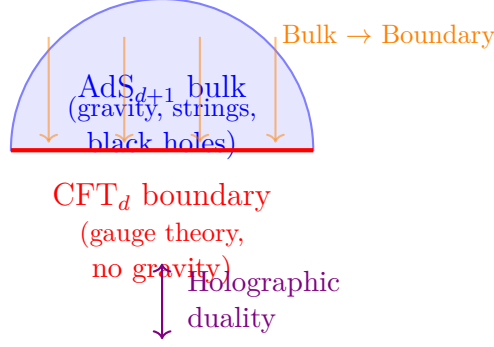- Bulk black hole $\leftrightarrow$ Thermal state in CFT

Figure 3.3: AdS/CFT holographic correspondence. Quantum gravity in $(d+1)$-dimensional Anti-de Sitter space (blue bulk) is dual to conformal field theory on d-dimensional boundary (red). Bulk physics encodes on lower-dimensional boundary.

3.4 Induced Geometry on Field Manifolds

3.4.1 Configuration Space Geometry

For field $\phi : M \to \mathbb{R}$, the space of all field configurations $\mathcal{C} = \{\phi\}$ forms infinite-dimensional manifold.

DeWitt metric on configuration space:

$$G_{\phi\phi'}[\delta\phi] = \int_M \sqrt{g}\, g^{\mu\nu} \delta\phi(x) \nabla_\mu \nabla_\nu \delta\phi'(x)\, d^dx \qquad (3.9)$$

where $\delta\phi$ is field variation.

3.4.2 Moduli Space and Vacuum Manifolds

For theories with spontaneous symmetry breaking, vacuum configurations form **moduli space** $\mathcal{M}_{\text{vac}}$:

$$\mathcal{M}_{\text{vac}} = \{\phi_{\text{vac}} : V(\phi_{\text{vac}}) = V_{\min}\}/G \qquad (3.10)$$

where $V(\phi)$ is potential and G is gauge/symmetry group.

Example: Mexican hat potential:

$$V(\phi) = \lambda(\phi^2 - v^2)^2 \qquad (3.11)$$

Vacuum manifold: $|\phi_{\text{vac}}| = v$, a circle S^1 with circumference $2\pi v$.

3.5 Dimensional Reduction via Field Condensates

3.5.1 Dimensional Compactification from Condensates

Consider 5D theory with scalar field $\Phi(x^\mu, y)$ where y is extra dimension. If Φ develops vacuum expectation value (VEV):

$$\langle \Phi(y) \rangle = \Phi_0 e^{iky} \qquad (3.12)$$

with $k = 1/R$, the vacuum becomes periodic with period $2\pi R$, effectively compactifying y on circle.

3.5.2 Topology Change via Phase Transitions

Field configurations can induce topology change. Consider Einstein-Hilbert action with scalar:

$$S = \int d^4x \sqrt{-g} \left[\frac{R}{16\pi G} - \frac{1}{2}(\partial\phi)^2 - V(\phi) \right] \tag{3.13}$$

For specific potentials $V(\phi)$, solutions exist with changing topology (wormholes, bubble nucleation).

3.6 Emergent Symmetries and Conservation Laws

3.6.1 Noether's Theorem and Emergent Currents

Symmetries need not be fundamental—they can emerge at low energies. For action $S[\phi]$ approximately invariant under $\phi \to \phi + \delta\phi$:

$$\delta S = \int d^d x \, \mathcal{L}_{\text{breaking}} \ll S \tag{3.14}$$

Approximate Noether current:

$$j^\mu = \frac{\partial \mathcal{L}}{\partial(\partial_\mu \phi)} \delta\phi - \mathcal{J}^\mu_{\text{breaking}} \tag{3.15}$$

with $\partial_\mu \mathcal{J}^\mu_{\text{breaking}} = \mathcal{L}_{\text{breaking}}$.

Example: Chiral symmetry in QCD: At energies $E \gg m_{\text{quark}}$, quark masses negligible. QCD Lagrangian has approximate $SU(2)_L \times SU(2)_R$ chiral symmetry, spontaneously broken to $SU(2)_V$ (isospin), giving rise to pions as pseudo-Goldstone bosons.

3.7 Quantum-to-Classical Transition

3.7.1 Decoherence and Geometric Emergence

Smooth classical geometry emerges from quantum superpositions via decoherence:

$$|\psi\rangle = \sum_i c_i |g_i\rangle \quad \xrightarrow{\text{decoherence}} \quad \rho = \sum_i |c_i|^2 |g_i\rangle\langle g_i| \tag{3.16}$$

where $|g_i\rangle$ are different geometric (metric) states.

Emergent classicality condition: Decoherence timescale τ_{dec} must be much shorter than observation time τ_{obs}:

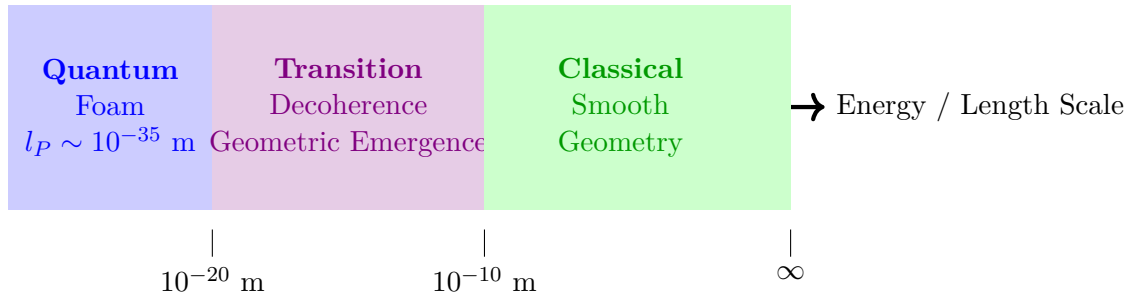$$\tau_{\text{dec}} \ll \tau_{\text{obs}} \tag{3.17}$$

Figure 3.4: Quantum-to-classical transition for spacetime geometry. At Planck scale (blue), quantum fluctuations dominate. Through decoherence (violet), superpositions collapse. At macroscopic scales (green), smooth classical geometry emerges.

3.8 Summary and Forward Bridge

This chapter explored how geometric structures emerge from underlying field dynamics:

Key Mechanisms:

- **Induced metrics** (Eq. **??**): Field gradients generate effective spacetime curvature
- **RG dimensional flow** (Eq. **??**): Effective dimension runs with energy scale
- **Holographic principle** (Eq. **??**): 3D information encoded on 2D surface
- **AdS/CFT** (Eq. **??**): Explicit gravity/gauge duality exhibiting holography
- **Decoherence** (Eq. **??**): Quantum-to-classical transition yielding definite geometry

Physical Insights:

- Geometry is not fundamental but emergent from field configurations
- Spacetime dimension varies with energy scale (spectral dimension)
- Bulk physics encodes on lower-dimensional boundaries (holography)
- Classical smoothness emerges via decoherence of quantum fluctuations

Wheeler's vision of geometry emerging from quantum dynamics finds concrete realization in holography, RG flow, and decoherence mechanisms. Chapter **??** extends this to field dynamics on fractal structures, exploring how scaling laws and critical phenomena govern behavior at multiple scales.

Chapter 4

Field Dynamics and Scaling Laws

The Hidden Order at Critical Points

In 1966, Leo Kadanoff introduced a revolutionary idea that would transform our understanding of phase transitions: at critical points, systems exhibit self-similarity across scales—behaving identically whether viewed at atomic, mesoscopic, or macroscopic resolution.

Consider water at its critical point ($T_c = 374$řC, $P_c = 218$ atm). Density fluctuations appear at all scales simultaneously—microscopic molecular clusters, mesoscopic droplets, macroscopic density variations all coexist. The system has no characteristic length scale; it is **fractal**.

Kadanoff's "block spin" picture: group spins into blocks, average to get effective spin, repeat. At criticality, this procedure leaves physics unchanged—hallmark of scale invariance and RG fixed point.

This chapter develops field dynamics on fractal and self-similar structures, deriving universal scaling laws governing critical phenomena, turbulence, and pattern formation.

4.1 Renormalization Group and Scaling Exponents

4.1.1 The RG Transformation

For field $\phi(\mathbf{x})$ with action $S[\phi]$, the RG transformation combines:
1. **Coarse-graining**: Integrate out short-distance modes $\phi_>$ with $k > \Lambda/b$
2. **Rescaling**: $\mathbf{x} \to b\mathbf{x}$, $\phi \to b^{-\zeta}\phi$ to restore cutoff Λ

RG flow equations:
$$\frac{dg_i}{d\ell} = \beta_i(\{g_j\}) \tag{4.1}$$

where $\ell = \log b$ is RG "time" and $\{g_i\}$ are coupling constants.

4.1.2 Critical Exponents and Universality

At RG fixed point, observables scale as power laws. Define **critical exponents**:
- **Correlation length**: $\xi \sim |T - T_c|^{-\nu}$
- **Magnetization**: $M \sim |T - T_c|^{\beta}$ (confusingly, β not beta function!)
- **Susceptibility**: $\chi \sim |T - T_c|^{-\gamma}$
- **Specific heat**: $C \sim |T - T_c|^{-\alpha}$
- **Correlation function**: $\langle \phi(0)\phi(\mathbf{r})\rangle \sim r^{-(d-2+\eta)}$

Scaling relations: Not all exponents independent. Equalities derived from RG:

$$\alpha + 2\beta + \gamma = 2 \quad \text{(Rushbrooke)} \tag{4.2}$$
$$\gamma = \nu(2 - \eta) \quad \text{(Fisher)} \tag{4.3}$$
$$d\nu = 2 - \alpha \quad \text{(Josephson)} \tag{4.4}$$

RG flow in coupling space
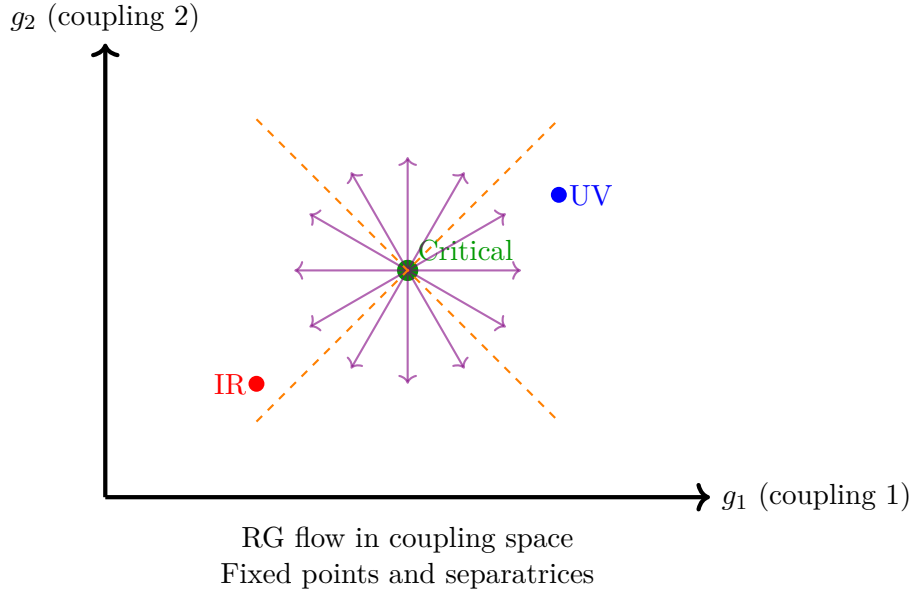Fixed points and separatrices

Figure 4.1: Renormalization group flow in coupling constant space. Fixed points (colored dots) attract or repel trajectories. Critical point (green) has mixed stability: stable along some directions (relevant operators), unstable along others (irrelevant operators).

4.2 Critical Exponents for Physical Systems

4.2.1 Ising Model (3D)

The 3D Ising model (ferromagnetic spins on cubic lattice) exhibits:

$$\nu \approx 0.630, \quad \beta \approx 0.327, \quad \gamma \approx 1.237, \quad \eta \approx 0.036 \tag{4.5}$$

4.2.2 XY Model and Kosterlitz-Thouless Transition

The 2D XY model (planar spins $\mathbf{S} = (\cos\theta, \sin\theta)$) exhibits **topological phase transition**:

$$\eta(T) = \begin{cases} 0 & T < T_{KT} \quad \text{(bound vortex pairs)} \\ 1/4 & T = T_{KT} \quad \text{(critical)} \\ > 1/4 & T > T_{KT} \quad \text{(free vortices)} \end{cases} \tag{4.6}$$

4.2.3 Turbulence and Kolmogorov Scaling

Fully developed 3D turbulence exhibits self-similar energy cascade with **Kolmogorov spectrum**:

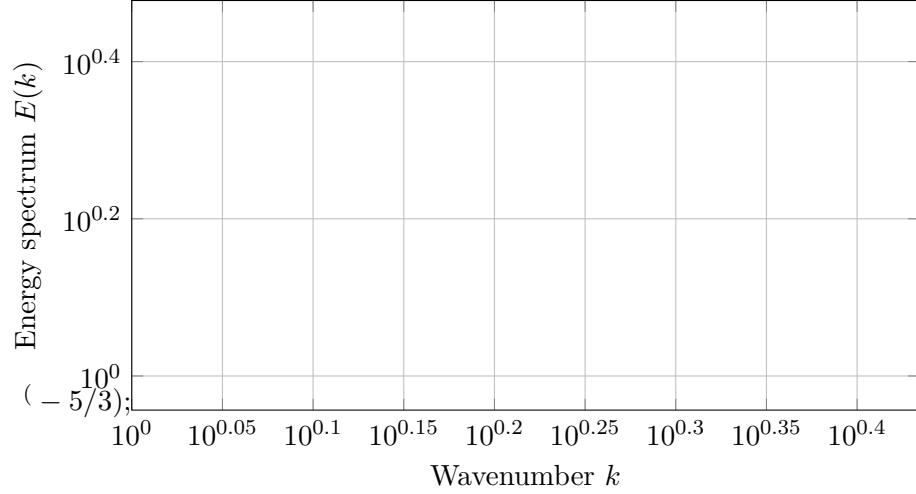$$E(k) = C_K \epsilon^{2/3} k^{-5/3} \tag{4.7}$$

Figure 4.2: Kolmogorov energy spectrum for 3D turbulence. Inertial range (green) exhibits $k^{-5/3}$ scaling, representing self-similar energy cascade from injection scale (red, left) to dissipation scale (red, right).

where ϵ is energy dissipation rate, k is wavenumber.

4.3 Fractal Field Configurations: Skyrmions and Instantons

4.3.1 Skyrmion Field Configuration

A **skyrmion** is topological soliton in 2D field theories. For unit vector field $\mathbf{n}(\mathbf{r}) : \mathbb{R}^2 \to S^2$:

$$\mathbf{n}(\mathbf{r}) = (\sin\Theta(\rho)\cos\varphi, \sin\Theta(\rho)\sin\varphi, \cos\Theta(\rho)) \tag{4.8}$$

with $\rho = |\mathbf{r}|$, $\varphi = \arg(x + iy)$, and profile $\Theta(\rho)$ satisfying:

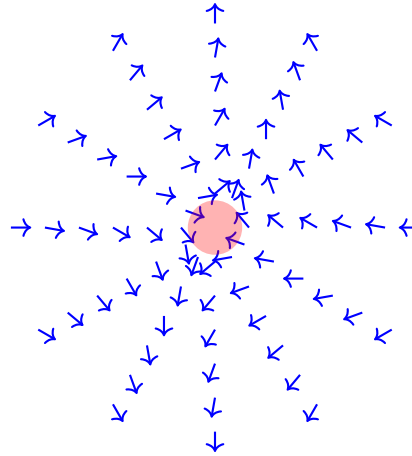$$\Theta(0) = \pi, \quad \Theta(\infty) = 0 \tag{4.9}$$

4.3.2 Instantons and Tunneling

Instantons are localized solutions to Euclidean field equations, describing quantum tunneling between vacua.

For double-well potential $V(\phi) = \lambda(\phi^2 - v^2)^2/4$, instanton solution:

$$\phi_{\text{inst}}(x, \tau) = v \tanh\left(\frac{m(x - x_0)}{\sqrt{2}}\right) \tag{4.10}$$

interpolating between vacua $\phi = -v$ (at $x \to -\infty$) and $\phi = +v$ (at $x \to +\infty$).

Skyrmion texture

Topological charge $Q = +1$

Figure 4.3: Skyrmion field configuration (2D vector field schematic). Spins (blue arrows) wind once around center. Topological charge $Q = +1$ protects configuration against smooth deformations.

4.4 Universality Classes and Classification

4.4.1 Symmetry and Dimension Determine Universality

Systems belong to same **universality class** if they share:
1. Spatial dimension d
2. Order parameter symmetry group G
3. Short-range vs long-range interactions

Common universality classes:

Class	Symmetry	$d = 2$	$d = 3$
Ising	$\mathbb{Z}_2$	$\nu = 1$	$\nu \approx 0.630$
XY	$O(2)$	$\nu_{\mathrm{KT}} = \infty$	$\nu \approx 0.672$
Heisenberg	$O(3)$	$\nu \approx 0.70$	$\nu \approx 0.710$
Percolation	Geometric	$\nu = 4/3$	$\nu \approx 0.875$

Table 4.1: Critical exponent ν for major universality classes in 2D and 3D. Exact results known for 2D Ising; 3D values from Monte Carlo simulations and ϵ-expansion.

4.5   Pattern Formation and Self-Organization

4.5.1   Reaction-Diffusion Systems

The **Gray-Scott model** for chemical pattern formation:

$$\frac{\partial u}{\partial t} = D_u \nabla^2 u - uv^2 + F(1-u) \tag{4.11}$$

$$\frac{\partial v}{\partial t} = D_v \nabla^2 v + uv^2 - (F+k)v \tag{4.12}$$

where u, v are concentrations, D_u, D_v diffusion constants, F feed rate, k removal rate.

4.5.2   Swift-Hohenberg Equation

Pattern formation near threshold described by **Swift-Hohenberg equation**:

$$\frac{\partial u}{\partial t} = \mu u - (\nabla^2 + q_c^2)^2 u + N[u] \tag{4.13}$$

where μ is control parameter, q_c critical wavenumber, $N[u]$ nonlinearity.

For μ slightly positive, striped patterns with wavelength $\lambda = 2\pi/q_c$ form spontaneously.

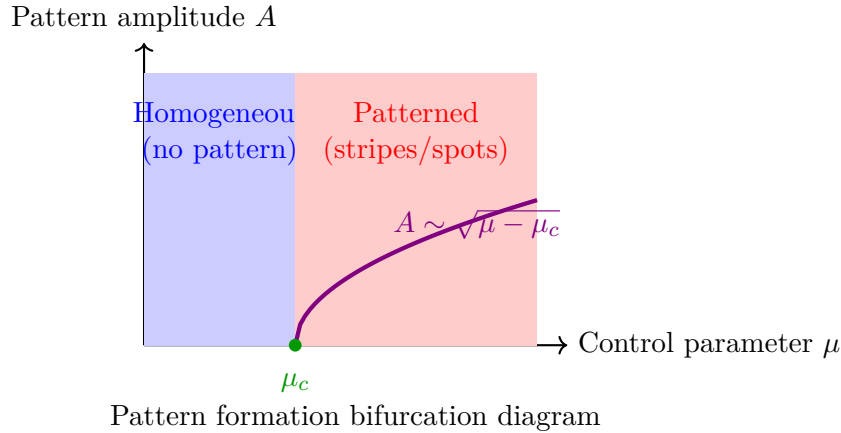Pattern formation bifurcation diagram

Figure 4.4: Pattern formation phase diagram (Swift-Hohenberg type). Below threshold $\mu < \mu_c$ (blue): homogeneous state stable. Above threshold (red): patterned state emerges with amplitude $A \sim \sqrt{\mu - \mu_c}$ (violet curve, supercritical bifurcation).

4.6   Multiscale Dynamics and Hierarchical Structures

4.6.1   Separation of Scales

Many systems exhibit dynamics at widely separated timescales:

$$\tau_{\text{micro}} \ll \tau_{\text{meso}} \ll \tau_{\text{macro}} \tag{4.14}$$

Adiabatic elimination: Fast variables x_{fast} equilibrate on τ_{micro}, can be integrated out, yielding effective dynamics for slow variables x_{slow} on τ_{macro}.

4.6.2   Hierarchical Field Theories

Multiscale systems described by nested field theories:

$$S_{\text{total}} = S_{\text{macro}}[\Phi] + S_{\text{meso}}[\phi|\Phi] + S_{\text{micro}}[\psi|\phi] \tag{4.15}$$

where each scale conditions on slower scales.

4.7   Summary and Concluding Remarks

This chapter developed field dynamics and scaling laws for fractal and self-similar systems:

Key Concepts:
- **Renormalization group** (Eq. **??**): Systematic coarse-graining revealing fixed points and universal behavior
- **Critical exponents**: Power-law scaling at phase transitions ($\nu, \beta, \gamma, \alpha, \eta, \delta$)
- **Universality classes**: Systems with same symmetry + dimension share exponents (Table **??**)
- **Kolmogorov spectrum** (Eq. **??**): $k^{-5/3}$ scaling in turbulent energy cascades
- **Topological solitons**: Skyrmions (Eq. **??**) and instantons with protected charge
- **Pattern formation**: Turing instability, Swift-Hohenberg equation, spontaneous symmetry breaking

Physical Applications:
- Phase transitions: ferromagnets, superfluids, liquid-gas (Ising universality)
- Turbulence: atmospheric flows, ocean currents, stellar convection
- Pattern formation: chemical reactions, biological morphogenesis, geological structures
- Topological matter: magnetic skyrmions, quantum Hall states, QCD vacuum

Unifying Themes:
- Scale invariance at critical points enables universal predictions
- Fractal structures emerge naturally from self-similar dynamics
- Topology provides protection against perturbations
- Multiscale physics requires hierarchical description

From Kadanoff's 1966 insight about blocked spins to modern applications in quantum materials and cosmology, scaling laws reveal deep connections between microscopic dynamics and macroscopic phenomena. The fractal geometry developed in Chapters **??**–**??** provides the natural mathematical language for these scale-invariant systems.

Forward connections: The techniques developed here—RG flows, scaling exponents, universality classes—apply broadly across theoretical physics, from condensed matter to quantum field theory to cosmology. Future work may extend fractal field dynamics to quantum gravity, where spacetime itself exhibits scale-dependent fractal structure.